(in a dual range ADC this is equivalent to 15 pC) for downstream scintillators (except for the beam region) and 1000 ADC counts for upstream scintillators (since upstream only get minimum ionizing particles).

Due to the large amount of light generated in the scintillators in the deflected beam region by heavy fragments, each beam region, used by three different physics programs (roughly 7 counters) were calibrated at a lower voltage setting, so that there would be no overflow in the FERA ADCs. As a result, we were unable to use the full range of dual range ADC's which can digitize upto $\sim$32K ADC counts (or 1600 pC). A typical Z=14 particle produced 10-15K ADC counts with the selected gain settings in these ADC's.

The gain calibration of the phototubes was done once prior to the data taking run and the calibrated voltages were loaded into the HV power supply for the phototubes before each physics program operated.

2 U/Cu Calorimeters

2.1 Construction

The main purpose of the U/Cu calorimeters are to provide information about the energy (E) of the beam rapidity nucleons going through the 0.8^o hole in the participant calorimeter. They should measure positions (X and Y) of the particles with reasonable accuracy and should be able to resolve multineutron or multiproton events where several neutrons or protons hit the calorimeter wall simultaneously. A good online energy resolution is essential to trigger on various peripheral channels.

To achieve these goals, U/Cu/Scint calorimeters built for ISR experiment R807 and subsequently used by HELIOS collaboration (CERN experiment NA34) were redesigned [42, 44] by replacing the electromagnetic section with one continuous hadronic section. In addition, the scintillator plates were optically decoupled to improve the ability to separate two showers in the same neighborhood. Although such a change would reduce the measured energy resolution of $0.35/\sqrt{E}$ in these calorimeters, the collaboration decided to sacrifice energy resolution for required spatial measurement capability.

Figure 2.5 shows a schematic drawing of the redesigned calorimeters. Longitudinally, each module consists of 40 identical sections, each with a 5 mm Cu plate and two 30 mm depleted uranium plates as an absorber, alternating with 2.5 mm scintillator sheets. The total depth of a stack is 4.2 absorber lengths. Light created in the scintillator is intercepted by wavelength shifter (WLS) bars parallel to the beam direction, 2.5 mm thick, 10 cm wide and 120 cm long. Each module has 24 WLS bars, 12 on each side of the stack and they are coupled to phototubes located in the back of the module. The phototubes used were EMI 9905B and phillips XP2081 except for the three calorimeters in the deflected beam region. In these regions we used Hamamatsu photo tubes.

Depending on the light decoupled sections of the scintillator plates we can separate

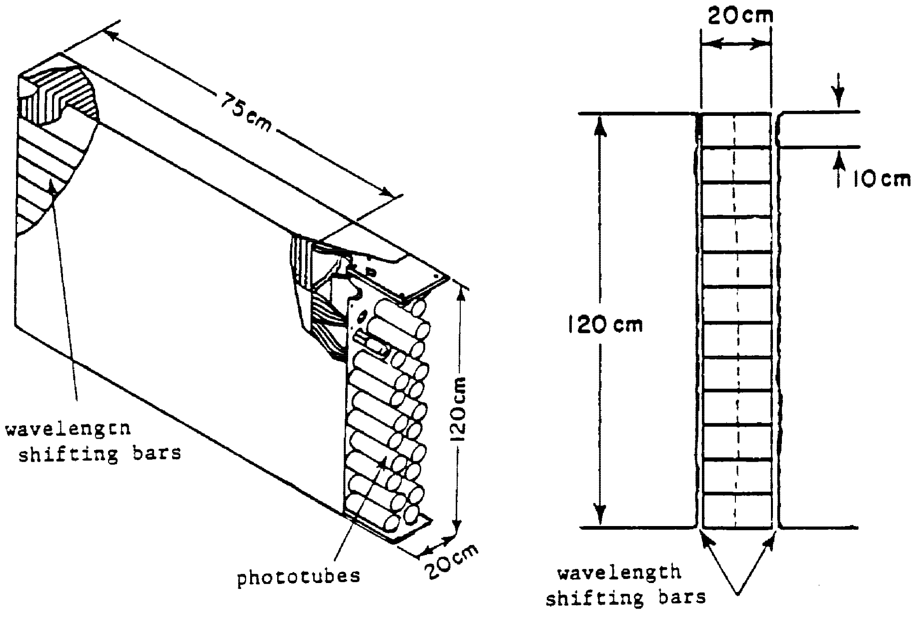

Figure 2.5: A U/Cu calorimeter module. Ref [44]

the 25 modules into three types. The first type consists of 3 modules which are used to detect protons. Each of these are divided into 24 sections of 10x10 cm^2 cells. The second type with no divisions consists of one module (beam calorimeter) placed directly in the Z/A=0.5 beam line. The rest of the modules consisting of 20x10 cm^2 size cells are used to detect neutrons, proton rich or neutron rich nuclei as well and π-neuts.

From each calorimeter module, anode signals of the photomultiplier tubes (each module has 24 photo tubes) were extracted and split into two. One of these signals was connected to a summing box which performs the analog sum of 24 signals over each calorimeter module. The other signal was connected to a Fastbus ADC (LeCroy model 1882) of 400 fC/channel. The output signals from the summing boxes were split into two and one signal was connected to the FERA ADC's (LeCroy model 4290) which were used in the trigger and the other signal was discriminated and connected to a TDC (LeCroy Model 4291B) system to extract timing from calorimeter modules.

2.2 Calibration

The gain equalization of each phototube in individual stacks was done using the radioactivity of the uranium plates in the calorimeter itself. Uranium plates create uniform low level light (uranium noise) in the scintillator plates. The gains of the phototubes can be adjusted so that the response of each tube to the uranium noise produces the same average DC current.

For the measurement of the average uranium current, a CAMAC module (current monitor) was designed and built. The current monitor contains a current-voltage conversion (CVC) followed by a voltage-frequency (VFC) conversion. The output of the VFC is connected to a scaler in each channel. Due to the possible signal ground problems which alter the measurement of the gain in each photo tube, one single phototube in each individual stack was completely covered (blackened phototube) to use as a reference and the calibration procedure was carried out as described below.

- Without turning the high voltages on the phototubes, the background noise signal was recorded for each tube.
- Phototube voltages were turned on and the new signals from each phototube were recorded. The shift in the signals from the blackened phototube was computed and each phototube signal was corrected by this amount in each module. This shift indicates the possible ground shifts due to the addition of voltage supplies assuming all phototubes produce roughly the same amount of dark currents.
- For three different voltage settings, current monitor readings were recorded and the gains in each tube due to the uranium light was calculated. With an extrapolation, a new voltage setting was calculated for each tube to bring the gain to the reference value.

This was done on an average, every 24 hours during the normal data taking runs. The reference reading was calculated by the response of these calorimeters to 12 GeV pion and muon beams.

Although there are a few corrections involved in the procedure, it was found that the method brings the phototube gains to the standard energy scale. The studies of gain drifts in phototubes is discussed in more detail in chapter 3.

3 Tracking Chambers

E814 operating conditions provided an important challenge for tracking detectors. They were required to operate in an environment with high track densities and high beam rates which can extend upto 1 MHz. In addition, they require a large dynamic range which begins with minimum ionizing particles and extends upto heavy fragments with Z=14. A detailed description of E814 tracking chambers is given elsewhere [45, 46] and only the relevant information to understand the performance of the drift chamber studies described in this thesis is given here.

3.1 Pad Chamber (DC1)

This detector, placed in between the two dipole magnets plays an essential role in this analysis. As shown in Figure 2.6 (a), it consists of a single cathode plane divided into a large number of rectangular pads. Anode wires are placed above the pads and field wires with slightly negative potential are placed in between the anode wires. All pads beneath one anode wire are interconnected by a resistive strip. An avalanche created by a charge particle traversing the detector induces a localized charge on several pads. Measurement of the induced charge on the pads, combined with an interpolation, provides an unambiguous measurement of the track position.

Depending on the track densities, the readout spacings vary over the plane of the chamber. Approximately, every 10th pad is readout by charge sensitive preamplifiers which are mounted on the chamber itself. Each preamplifier output passes through a pair of transformers into a shaping amplifier which produces a bipolar pulse of 200 nsec risetime and this is digitized by a 15-bit LeCroy model 1885F dual range ADC system.

The active area of the chamber is 26x16 cm^2. The anode wire spacing is 4 mm and the separation between readout nodes range from 15 mm (edges) to 6 mm (center) giving a total of 1016 channels. Detector thickness is about 6% radiation length. With collimated x-ray beams, a position resolution of $\approx$ 70 μm was observed.

3.2 Drift Chambers (DC2 and DC3)

The drift chambers DC2 and DC3 consist of 6 drift planes followed by a single layer of chevron shaped pad plane as shown in Figure 2.6 (b). The corresponding wires in adjacent drift planes are shifted by half of the separation between wires in a single plane to eliminate the effects of left-right ambiguity in track reconstruction. An aluminized milar layer is inserted in each drift section to absorb the low energy δ rays.

Signals from each anode wire are connected to low noise preamplifiers. The output of the preamplifier is connected to a unipolar shaping amplifier which has a gain of $2x10^3$ and a risetime of 12 nsec. The output of the shaping amplifier enters a dual discriminator in which the lower level sensitive to the leading edge of the signal generated by the drift cloud and the upper level which is blind to minimum ionizing tracks, measure the centroid of the charge distribution of heavily ionizing tracks (zero-crossing discriminator). The upper level shapes the 12 nsec unipolar pulse into a 60 nsec risetime bipolar pulse before the signal enters the zero-crossing discriminator with a gain of $\sim$ 1 at the shaping stage. The output of the dual discriminator is connected to a 10-bit, pipeline, LeCroy 1879 TDC with 1 nsec resolution. Signals from the cathode plane follow the same path as DC1 signals.

The active size of these chambers are 10x50 cm^2 and 20x100 cm^2 respectively, and they are identical in design. DC2 has 128 wires in each driftplane with a separation of 6.35 mm. Its pad plane has a total of 464 chevron pads with variable density ranging from 3 mm to 9 mm. DC3 has 160 wires in each driftplane with a 12.70 mm separation and a total of 760 pads whose sizes range from 5 mm to 15 mm. The thickness of DC2 and DC3 is about 10% and 20% radiation lengths respectively. Both chambers were expected to provide a 200 μm single cell resolution in the X direction and the chevron pads were expected to provide a resolution of approximately 1-3% of the spacing between readout nodes in the Y direction.

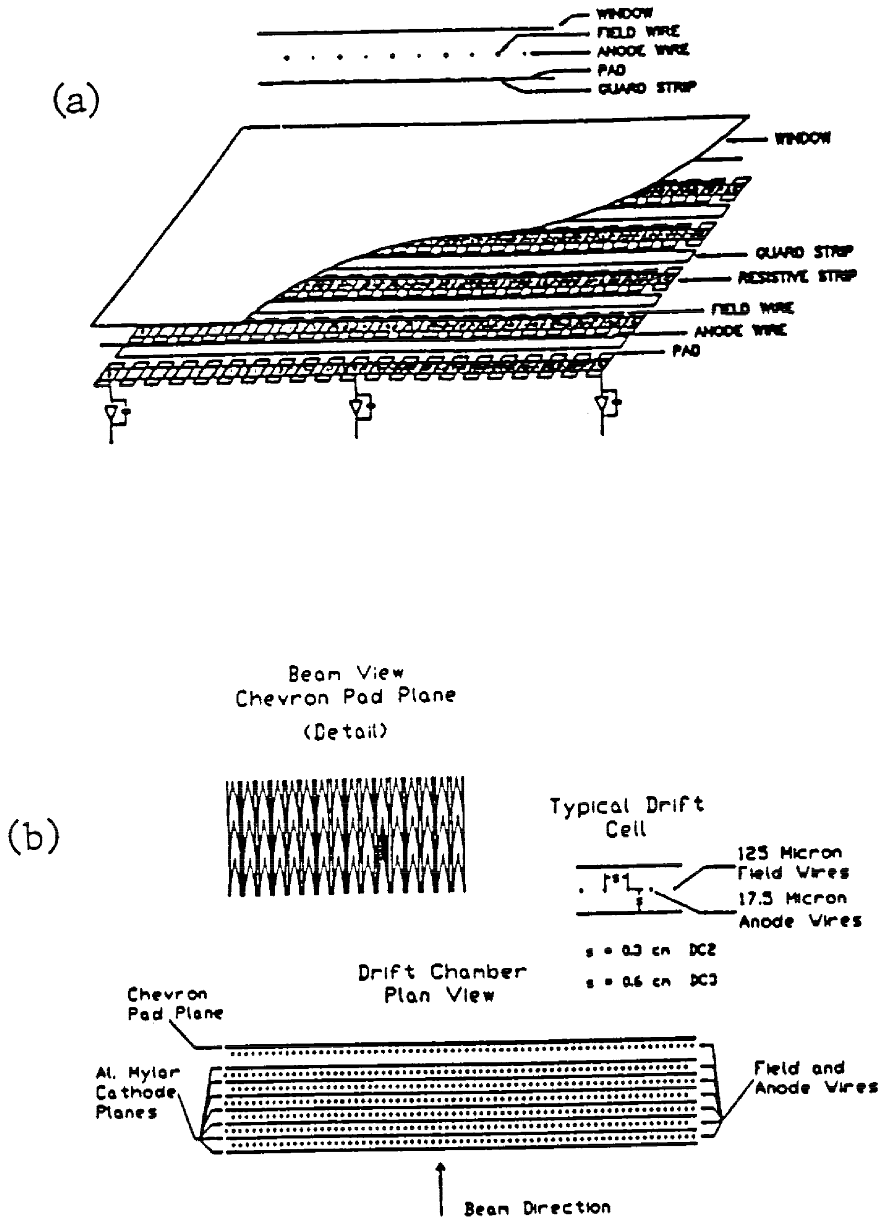

Figure 2.6: The E814 tracking chambers. (a) A view of the pad chamber DC1 showing the locations of the anode wires and field wires. (b) A view of the drift chamber DC2 (and DC3) showing the chevron pad plane and the drift region. Ref [46]

3.3 Calibration

The drift cells operate by measuring the time between the passage of an ionizing particle and the subsequent avalanche around the anode wire. Thus, at the calibration phase, the relative (channel-to-channel) time delays of each channel are measured and recorded. In the offline analysis, adjustments are made to the calibration constants to correct for variations in time at the reduced gain region.

The pad chambers operate by measuring the image charge on a segmented cathode plane facing a standard drift wire. The centroid of the image charge distribution is inferred by measuring the relative charge accumulated on neighboring pads. Thus, the important parameters in the pad chamber calibration are the gain and pedestal of each channel. Since the charge signals are measured by 1885F dual-range ADC's, each channel must be calibrated independently for the two ranges.

A free-running pulser was used as a trigger for the data acquisition system and for a calibration pulser. The trigger pulses were delayed considerably before entering the data acquisition system. An adjustable delay between the trigger pulser and the calibration pulser was used to time the chamber's signals with the gates generated by the DAQ. The pulse height of the calibration pulser is controlled via a DAC resident in CAMAC. A system of CAMAC-controlled switches are used to ship the calibrated timed pulses to small regions of each chamber. The system is controlled by the same micro-VAX as is used for the data acquisition, but is run independently of the normal data acquisition since the normal DAQ does not provide the facility to program the calibration pulser during data taking.

During drift cell time calibration, the settings of the discriminator thresholds for each channel are also recorded with the measured time for the timed pulses. This was accomplished by recording the response to different pulser amplitudes. Tests have shown that the time value at threshold and the time value well above the threshold create the same relative time calibration for all channels due to the coarse (2 nsec/channel) digitization of the time.

The pad chamber calibrations are achieved by recording the response of channels to different pulse amplitudes. The low range and the high range of the ADC's are calibrated separately. The pedestal values are obtained from a set of "empty events" taken without pulsing the chambers. This method is required by the fact that there is a slight DC offset between the DAC (located in the counting house) and the calibration pulser (located near the chambers).

The calibration procedure is fully automated (with the exception of occasional gate timing and panel switch attenuator) and requires approximately 1 hour. This is executed before the data taking run.

CHAPTER 3

Detector Studies

In experimental physics, the quality of the results depends on the resolution of the detectors used. Due to various factors, the resolution of the detectors, achieved through bench tests is degraded in the experimental environment. For this reason, understanding the performance of the detectors, and, the corrections for factors contributing to degrade the resolution, plays a very important role. Studies to achieve the optimum resolution for Forward Scintillators, U/Cu Calorimeters and Tracking Chambers are described in detail in this chapter.

A Forward Scintillators

The Forward Scintillation counters are expected to provide a resolution which separates all charges from Z=1 to Z=14. This requires the offline analysis to obtain an optimum resolution from these counters. The counters located at the deflected beam region suffer more than the counters in other regions from rate dependence problems. Therefore corrections which are applied to obtain the best possible resolution for these counters are described.

1 Noise Corrections

1.1 60Hz corrections

The gain setting in the PM tubes in the deflected beam region counters provides a signal of about 5 pC for minimum ionizing particles. In order to obtain a good resolution for these particles, a pedestal (integrated noise when there is no signal) width of less than 1 pC is required. However, during the test runs, signals from these counters showed a pick up noise from power cables corresponding to a 60Hz ripple which is approximately 2-3 pC. This ripple scaled with the gain setting in each region can seriously compromise the signal resolution.

Because of our sensitivity to the 60Hz ripple, we used a special CAMAC unit to measure the position of the 60Hz waveform for every event. The measured position together with the event records were written in the data tapes. The CAMAC unit is a four channel, 24-bit scaler, whose contents are stored in a register upon receiving a signal (in this the case the pre-trigger), with 4 μsec accuracy. The scaler contents are cleared with a signal, derived from a zerocrossing discriminator which views the 60Hz waveform.

Figure 3.1 (a) shows a scatter plot of the signal (pulse height) obtained from one end of the forward scintillators in the beam region, against the measured position of the 60Hz ripple, when no beam particle is present in the apparatus (MT event). In this scale, minimum ionizing particles produce a signal of around 100 counts.

The shift in the pulse height for any location of the 60Hz ripple, for each signal, was evaluated by fitting orthogonal (Tschebyschev) polynomials for waveforms similar to the one shown, generated from each signal and corrected on an event by event basis. This removed the major noise contribution in the forward scintillator signals. However, even after correcting for the 60Hz ripple, a small component of the noise was present in each signal. This noise was correlated to the noise in signals of the neighboring counters which share common grounds in the electronics in the counting house. An additional correction was applied by computing the average noise in a physical group of signal cables. Only the signals which did not show a "hit" was used to calculate the noise average. A pedestal width of $\sigma \sim 2$ ADC counts (0.1 pC) was achieved after the correction.

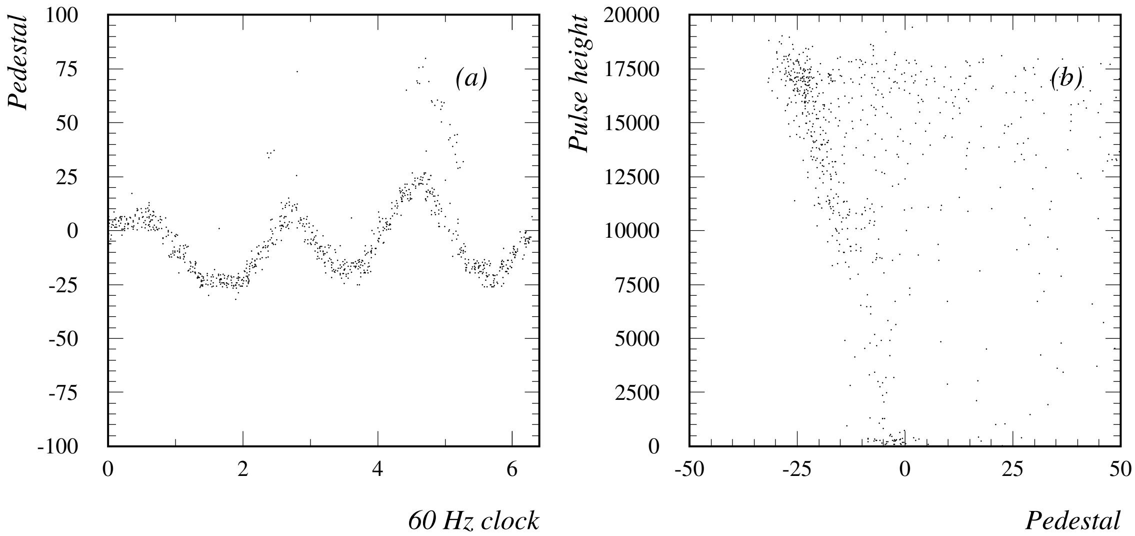

Figure 3.1: Noise in forward scintillators. (a) Effect due to the 60Hz ripple. (b) Cross-talk between nearest neighbors.

1.2 Cross-talk corrections

When real beam particles traversed the scintillators, an additional broadening was observed in the beam region counters. This effect caused a negative shift in the pedestals which was most prominent in the counter adjoining the counter in which the beam passed. A close inspection showed that this effect arises due to the cross-talk in the current monitors. [1] Whenever a beam particle or a high Z particle passes through a scintillator, the signal going through the current monitor induces an inverse polarity signal in its neighbors, causing this effect.

Figure 3.1 (b) shows the signal at one end of the scintillation counter through which the beam passes (DB counter) against its closest neighbor. A typical beam particle produces a negative shift of about 20-40 ADC counts in the closest neighbor. This effect was corrected by searching the counter which has the largest signal, and estimating the negative shift with a linear extrapolation to the signal height. The induced noise decreased with the distance from the beam counter and was present in about 8 counters surrounding the DB counter (4 to each side). After correction, a pedestal width of $\sigma \approx$ 3-5 ADC counts (0.15-0.25 pC) was achieved for beam region counters.

2 Charge Measurement

When a fast moving charge particle passes through a scintillation counter, it deposits an energy that is proportional to the square of its charge in the scintillation material. This energy is transformed into a pulse of light which travels along the scintillation counter. This can be detected and amplified by photomultiplier tubes placed at each end of the counter. We need to investigate how we can relate these signals and thereby extract the charge of the particle.

Consider a simple model of a scintillation counter with photo tubes attached at each end. Let x be the distance along the scintillator from the center to the point through which the charge particle traversed. The pulse height measured at the two ends can be written as,

$$Q_1 = LG_1 \exp\left[-\frac{(s+x)}{D}\right]$$

$$Q_2 = LG_2 \exp\left[-\frac{(s-x)}{D}\right]$$

assuming a pure exponential light attenuation in the light guide and the scintillator. Here, L is the light produced in the scintillator by the charged particle, G_1 and G_2 are the gains of the phototubes, s is the half length of the scintillator and D is the attenuation length of the scintillator. By taking the geometrical mean of pulse heights we get,

$$\sqrt{Q_1 Q_2} = L\sqrt{G_1 G_2} \exp\left[-\frac{s}{D}\right]$$

which is independent of the hit location of the particle and depends purely on the gains, and the amount of light (which is proportional to Z^2) that is produced in the scintillator.

[1] see chapter 2, section 2.2

Figure 3.2 shows the measured charge distributions for low Z particles in the forward scintillators obtained by evaluating the geometrical mean. In this scale, the gains were normalized to place minimum ionizing particles at 100 counts. The distribution shows a characteristic Landau shape.

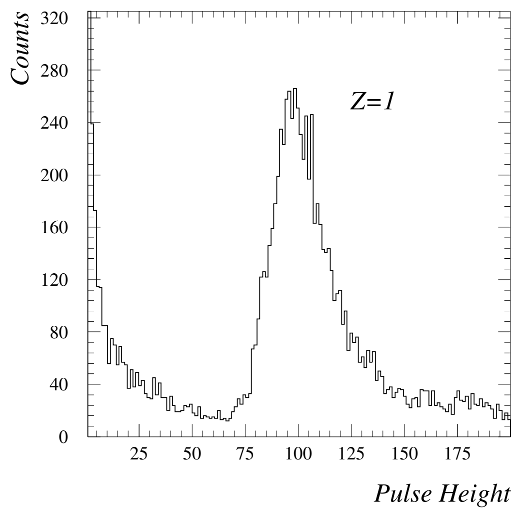

Figure 3.2: Measured pulse height in upstream forward scintillators for minimum ionizing particles.

3 Saturation Effects

For high Z fragments, the scintillators show a deviation from the expected Z^2 behavior. Although the specific mechanisms are not known, this effect has been discussed by many authors [47, 48]. The simplest model divides the ionization energy loss into two regions, the "core" and the "halo". The core is a region of high ionization density around the charge particle path, causing "saturation" or decrease in scintillation efficiency due to an enhancement in non radiative decay channels. The halo is a much larger region of low energy density surrounding the core that is energized by δ rays that are created in close collisions with the charge particle and suffers no saturation.

We used the simple parametrization suggested by Birks [49] for heavily ionizing particles at low velocities given by,

$$\frac{dL}{dX} = \frac{A(dE/dX)}{1 + B(dE/dX)}$$

where (dL/dX) is proportional to the amount of light produced for a particle of given ionization dE/dX, and A and B are two parameters which depend on the scintillator material. For 16 counters in the beam region (11 vertical and 5 horizontal) the parameters A and B were evaluated and corrected for this effect, by inverting the above formula. Table 3.1 shows the extracted parameters A and B, for 3 counters in the horizontal scintillator hodoscope and 5 counters in the vertical scintillator hodoscope in the deflected beam region. Although the constants A and B should be the same for a given scintillator material, a variation was observed among NE104 scintillators. This could be induced by the gain variations in the photomultipliers.

Table 3.1: The extracted parameters A and B using Birk's parametrization for a set of scintillator materials

Counter	Scintillator	A	B x1E-3
8	NE104	19.69	0.79
9	Bicron 400	19.77	1.60
10	NE104	19.67	0.59
24	NE104	19.69	0.76
25	NE104	19.66	0.49
26	NE104	19.67	0.56
27	NE104	19.67	0.64
28	NE104	19.67	0.64

Figure 3.3 (a) shows a measured charge distribution from the downstream silicon detector, against a measured charge from one of the forward scintillators in the beam region. The events that lie along the 45 degree line correspond to good candidates and the horizontal band of events corresponds to the downstream interaction products. Since the Si detector response is proportional to Z^2, the deviation from the 45 degree line indicates the scintillator saturation. Figure 3.3 (b) shows the same counter after correcting for the saturation effect. Resolution of $\sim$4.0% was observed for Z=14 particles in individual counters. The non uniformity in thickness along the counter length, and the phototube gain variations during the spill have not been taken into account in this analysis.

4 Time of flight

4.1 Slewing Corrections

If we consider the same model described in section 2, and assume a constant velocity v of light in the scintillator, the measured timing at the two ends can be written as

$$T_1 = \bar{T} + \frac{(s+x)}{v}$$

$$T_2 = \bar{T} + \frac{(s-x)}{v}$$

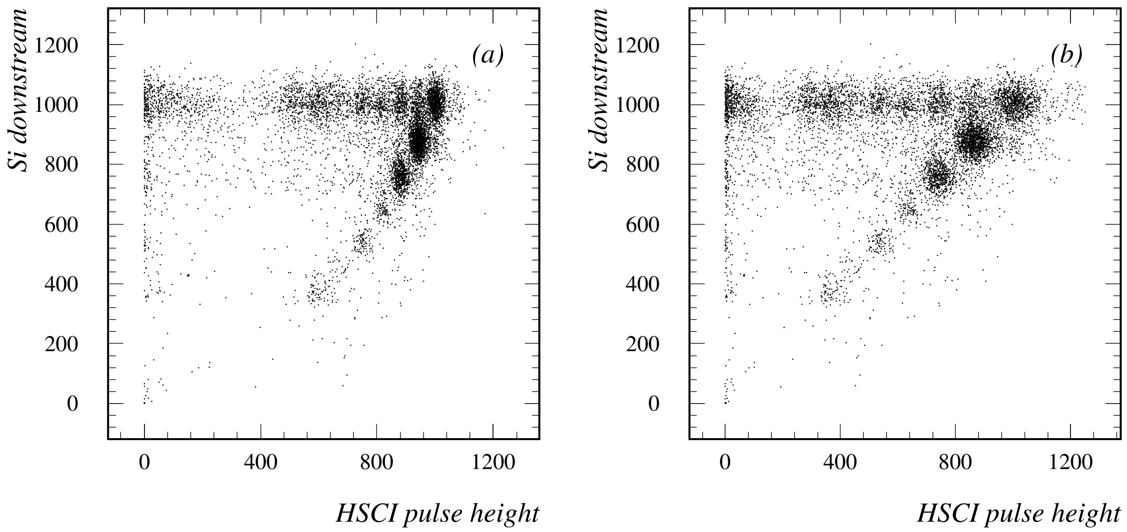

Figure 3.3: Effect of scintillator saturation. (a) Pulse height in Si downstream vs. measured pulse height in a scintillator. (b) Same after correcting for the scintillator saturation.

where $\bar{T}$ is the time of arrival of the particle at the counter. For simplicity, constant time offsets, such as phototube transit times, cable lengths and delays in the electronics are omitted from this discussion. By taking the average we get,

$$\frac{T_1 + T_2}{2} = \bar{T} + \frac{s}{v}$$

which is independent of the hit position and, since s/v is a constant, provides a measurement of the time of arrival of the particle.

This simple formula does not take into account the dependence of measured time on pulse height when leading-edge discriminators are used (slewing). Figure 3.4 (a) shows the measured pulse height against the measured time for one end of a counter. Leading-edge discriminators fire whenever the leading edge of the signal rises above a given threshold. When the signal becomes larger, the time to cross a given threshold becomes smaller, producing this effect. The corrections for the slewing effects have been discussed by many authors [50, 51], and following their arguments the corrected time was defined as,

$$T_c = T_1 + (A + \frac{B}{\sqrt{Q_1}})$$

where A and B are constants. The constant A (which accounts for the time offsets omitted in the previous discussion) is added to shift the time distribution to be centered at zero in order to simplify the cuts used in this analysis. Figure 3.4 (b) shows $1/\sqrt{Q_1}$ against the measured time for the same end of the counter. A linear relationship was observed justifying the above equation. For each phototube, the parameters A and B were computed and corrected for the slewing.

The time of flight distributions, computed by taking the average of T_1 and T_2 after correcting for the slewing effects for the counters in the beam region and the counters in the upstream proton region, yield a resolution of 350 ps and 215 ps respectively.

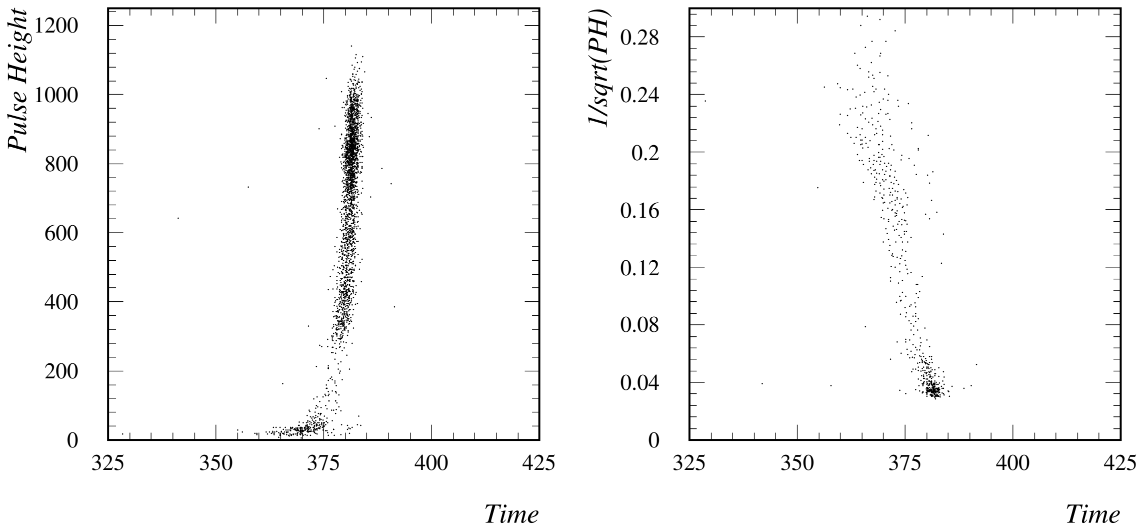

Figure 3.4: Effect due to slewing for time measurement. (a) Pulse height vs. time. (b) 1/sqrt(PH) vs. time demonstrating a linear relationship.

4.2 T-zero corrections

An additional contribution to the width of the timing signal comes from the time jitter associated with the start timing (T-zero) of the experiment obtained through one of the S4 signals. This effect can be corrected by taking the average of S4 timing signals. This correction was applied only to the upstream scintillator hodoscope where the highest resolution was required to identify prompt signals from albedo signals (background noise from particles scattering backwards) coming from the upstream calorimeter modules which are located roughly about 1.0 m from the upstream forward scintillators. A resolution of $\approx$ 200 ps was observed for upstream counters after all corrections were made.

5 Position Measurement

5.1 Position by pulse height

If we take the ratio of the expressions given in section 2 for the pulse height measured at the two ends of a counter, we get,

$$x = \frac{D}{2}\left[\ln(Q_2/Q_1) + \ln(G_1/G_2)\right]$$

which is a direct measure of the position along the scintillator. For every counter, $\ln(G_1/G_2)$ was estimated by centering the position distributions at x=0. The attenuation lengths D for NE104 and Bicron 400 scintillators are 120 cm and 200 cm respectively. By this method, a position resolution of 2 cm was obtained.

5.2 Position by timing

If we consider the expressions given in section 4 for timing measurements, we can write,

$$x = \frac{v}{2}(T_1 - T_2)$$

which gives an independent measurement of a position along the scintillator. The light velocity v inside the scintillator was found to be 18.75 cm/ns for NE104 and 15.0 cm/ns for Bicron 400. This measurement gave a position resolution of 2.5 cm.

Although these two measurements provide us with position measurements of very similar resolutions, the position obtained using time difference was more immune to gain drifts and worked better even in an environment with δ rays (given that the δ rays go through the counter in the vicinity of the particle position which we are measuring). Position by pulse heights are useful in the deflected region counters where TDC thresholds are marginal for minimum ionizing particles due to low gain setting in the PM tubes.

The position resolution in the direction perpendicular to the long dimension of the scintillators was taken as half width of the scintillation plates used.

B U/Cu Calorimeters

The performance of U/Cu calorimeters with test beam data has been described elsewhere [44]. In this section, the offline corrections which are applied to obtain optimum resolution with peripheral 1p and 1n events are described. In addition, studies on gain drifts and response to ^{28}Si beams are given.

1 PM gain drifts

The photomultiplier gain stability is a major factor contributing to the energy resolution in U/Cu calorimeters. During the normal data taking period, the accelerator, which delivers the beam to the experiment, fails to provide an uninterrupted beam throughout the run. The sudden changes in the working conditions affect the photo tube gains, degrading the resolution. In addition, it affects the trigger condition significantly since, to make decisions, the trigger relies on the energy measurement. This imposes a severe limitation on the choice of photomultipliers available in the market.

We have developed a photomultiplier test setup which simulates the AGS operating conditions. Figure 3.5 shows a schematic of the test setup. The background uranium noise for the phototubes was simulated with a slow pulse (red LED) of frequency ~1 sec and the light generated by a true beam particle was simulated with a fast pulse (green LED) of frequency ~1 μsec, both of which could be controlled externally through a PC driven data acquisition system. Phototubes were mounted inside a light-tight box, and the anode signals were connected to a 2280 ADC system via current monitors. Using this test setup, up to 55 individual photo tubes could be tested simultaneously. These tests consist of exposing the phototubes to 4 different conditions given by fast and slow pulses. The stability of the fast pulse was monitored by a reference photomultiplier which is exposed solely to the fast pulse. The temperature inside the box was monitored constantly by a temperature sensor mounted next to the slow pulse.

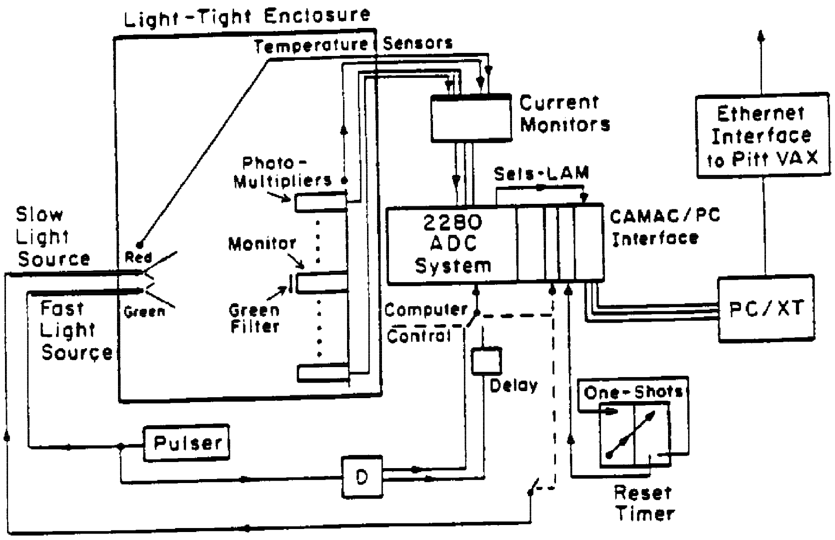

Figure 3.5: Pitt photomultiplier test facility with data acquisition setup.

We carried out tests for 100 R580-16 Hamamatsu photomultipliers. Our tests confirmed that, even for currents as high as 200 μA the short term gain variations are less than 1%. Figures 3.6 (a) and (b) show a long term variation of two of the Hamamatsu tubes. Although the short term variations of the two phototubes are similar to each other, the long term variations in one phototube is twice as large as in the other. The tubes which show minimum variation were selected by this test facility and used in places where heavy average currents and abrupt changes in running conditions are expected (Primarily in the deflected beam region).

2 Noise corrections

Although the calorimeters are calibrated every 24 hours, due to signal ground shifts, the energy measurements varied between calibrations. Any variation in the High Voltage power usage between calibrations can introduce shifts which are not present at

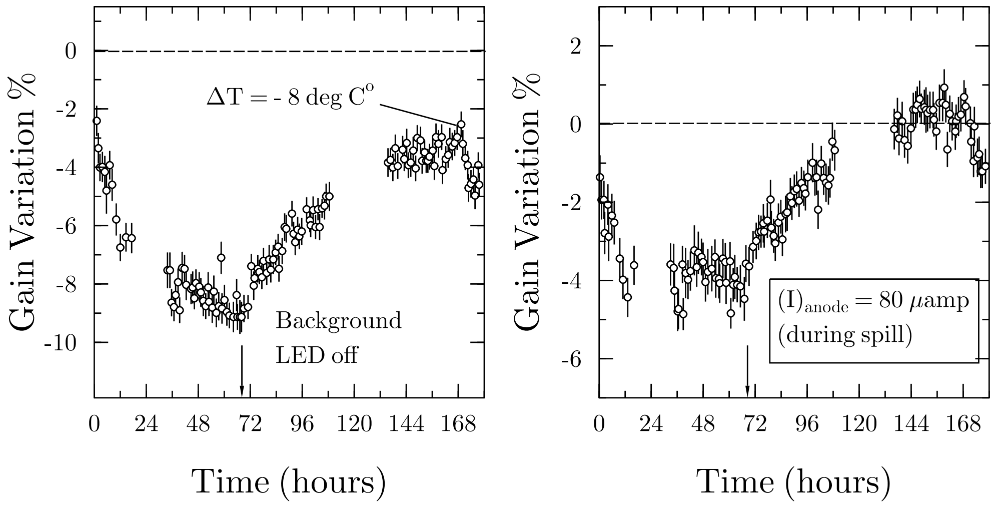

Figure 3.6: Gain drifts in two hamamatsu photomultiplier tubes.

the time at which the calibration takes place. In addition, any faults in the calibration procedure due to noise problems could change the absolute energy calibration.

The blackened photo tube, which does not see any light generated either by real particle showers or uranium noise, gives us an excellent system to monitor the effects of signal ground shifts over a large period of time. This effect was corrected event by event between calibration runs, assuming the blackened phototube pedestal shift as the true pedestal shift in all photo tubes in the offline analysis.

3 Cluster Finding

Cluster finding in the UCALs play a very important role in determining the energy of the incoming particle. Hadronic showers in our calorimeter modules usually extend over several towers of 10x10 cm^2 area and a cluster finding algorithm should recognize the towers which contain the real energy deposit. Energy sharing between showers due to multiple hits in the same vicinity or energy leakage due to the cracks between the calorimeter modules, complicate this analysis.

In the proton and the neutron calorimeters, the cluster search was performed in a very similar fashion. Initially, the number of clusters was identified by selecting the number of cells having an energy above a given threshold. Here, a cell refers to a light decoupled section. For proton and neutron calorimeters, the threshold energy was defined as 5.0 GeV. The total raw energy was computed by adding all signals together and this was compared with the expected energy which was calculated using the hit multiplicity, assuming each particle will deposit an energy of 13.8 GeV in the calorimeter. If the raw energy exceeded the expected energy by more than 2σ, where σ was taken to be $0.35/\sqrt{E}$, more clusters were searched until the expected energy was within 2σ of the raw energy. This procedure was introduced so that clusters which deposit a low energy in the hit cell, due to shower fluctuations or to particles going through the cracks between calorimeter modules, would not be overlooked.

The cluster energy was computed by taking the energy summed over a 3x3 cell area. Cells which share the energy between clusters were marked and this energy was divided among the clusters, but the main cell (cell in the middle) energy was not allowed to be shared between clusters. Finally, an additional check was made on each cluster to identify the events in which two particles passed through the same cell but were identified as one. Clusters in which this occurred were split and marked as two clusters. Figures 3.7 (a) and (b) show the measured raw energy distributions for protons and neutrons where the cluster analysis was performed. An energy resolution of $\sigma_E/E = 0.8/\sqrt{E}$ (where E is measured in GeV) was observed after the cluster analysis.

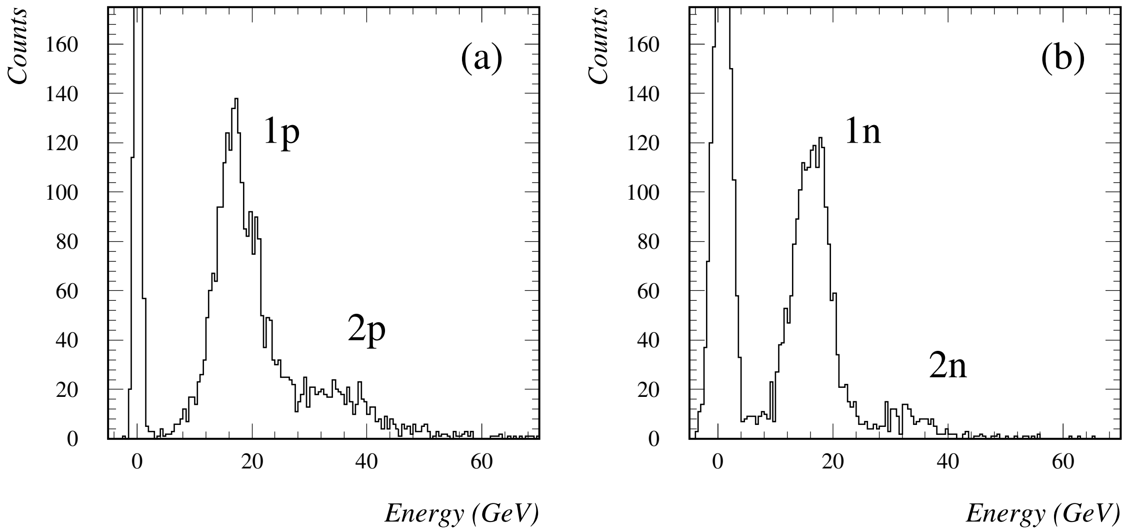

Figure 3.7: The measured raw energy distributions. (a) Protons. (b) Neutrons.

The energy deposited in the deflected beam region by pure beam particles or heavy ion fragments extended roughly over 5 calorimeter modules and hence no cluster analysis was performed. In this region, the energy was computed by taking the raw sum over 5 calorimeter modules surrounding the module with the maximum energy (hit module).

4 Position Measurement

The information about the hit position of the particles in these calorimeters can be extracted by using the energy deposited in the cells surrounding the hit cell. Out of various possible combinations, we have selected the form,

$$POS = A \times \ln\left(\frac{E_1}{E_2}\right)$$

To evaluate the X position in neutron calorimeters, two phototubes viewing the hit tower were selected as E_1 and E_2. For proton calorimeters, two cells to the left and the right of the hit cell were selected and for the beam region, two towers in the neighboring calorimeters were selected. The constant A was found to be 9.5, 1.5 and 2.8 for the neutron, the proton and the beam region calorimeters respectively. The formula to extract the X position given in reference [44] works equally well for these calorimeter modules.

For the Y position estimate, the towers above and below the hit tower were selected for E_1 and E_2 in the neutron and the beam region calorimeters. In the proton region calorimeters, the top and bottom cells were selected. The extracted values for the constant A are 1.8, 1.5 and 2.2 for the neutron, the proton and the beam region calorimeters respectively. For the beam calorimeter, which is a totally unsegmented module, an additional factor of 2.3 was used, bringing the constant to be roughly 5.1. A position resolution of 2.0 cm and 2.5 cm for X and Y respectively, was obtained for the neutron calorimeters. Similar position resolutions were observed for the proton region and beam region calorimeters.

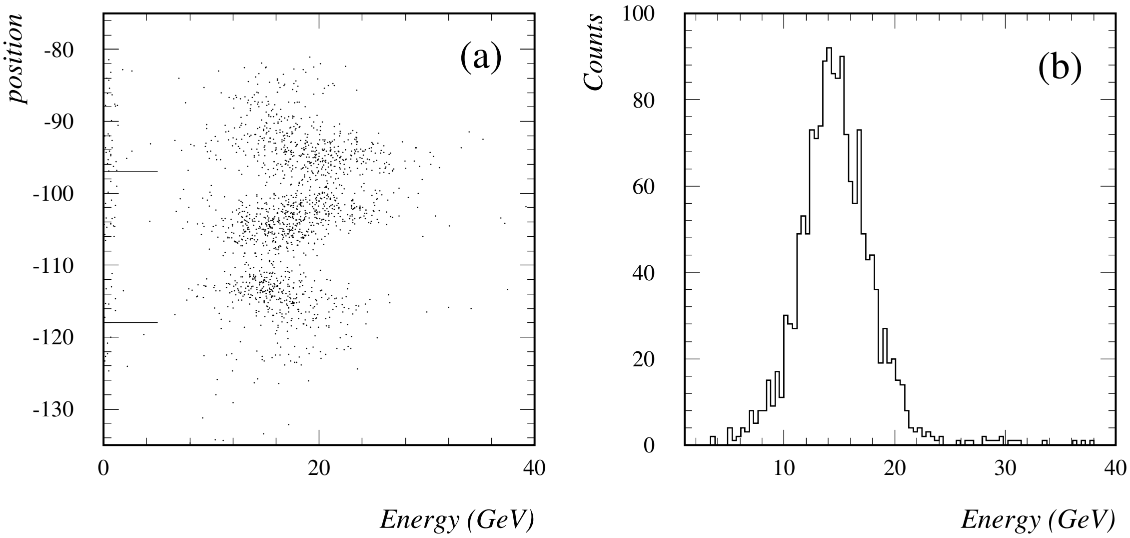

Figure 3.8: Position dependence on measured energy. (a) Position vs. energy. (b) Corrected energy distribution.

5 Energy Resolution

In order to achieve the maximum resolution from the calorimeters, it was necessary to correct for position dependent response. Figure 3.8 (a) shows the measured X position against the measured cluster energy for peripheral protons. The two pointers indicate the location of the cracks between the calorimeter modules. This plot shows that the calorimeter response is low for showers which originate at the center and that it increases steadily when it moves towards the edge of each calorimeter module.

By assuming the relationship between the position and the measured energy to be linear for a given energy, the following correction was applied on the measured energy.

$$E_c = E\left(1 - x\frac{A}{E}\right)$$

Figure 3.8 (b) shows the corrected energy distribution after all the corrections were made. This correction improves the resolution to $\sigma_E/E = 0.6/\sqrt{E}$. This is still higher than the value of $0.35/\sqrt{E}$ seen for the calorimeters when they were segmented longitudinally into an EM and hadronic sections [44]. No dependence of the response on the Y position was observed.

6 Shower Fluctuations

Among the factors that contribute in degrading a calorimeter resolution, the response of a calorimeter to a pure electromagnetic and to pure hadronic showers (e/π ratio) plays a very important role. [52, 53]. Particles deposit their energy as electromagnetic and as hadronic showers. Electromagnetic showers are well concentrated in the direction of the path of the particle compared to the hadronic showers which spread more in the lateral direction. In addition, electromagnetic showers produce a better energy resolution than hadronic showers due to smaller shower fluctuations. Depending on the fraction of the electromagnetic to the hadronic energy in the created shower, the response of the calorimeter can fluctuate (unless e/π=1).

Figure 3.9 (a) shows a scatter plot of maximum cell energy against the cluster energy computed for peripheral neutrons. This plot indicates that the concentrated showers produce more energy than the showers which are spread out among several cells. A recipe for correcting this effect can be found in the literature [54] and with a slight modification to fit our data is,

$$\bar{f}_i = Af_i\left(1 - f_i\frac{B}{\sqrt{E}}\right)$$

where A=1.23 and B=0.15 are constants found by minimizing the $\chi 2$ to force the sum of the $\bar{f}_i$ to be 13.8 GeV where i refers to the individual phototubes. Here, E is the total cluster energy, f_i is the individual readings from each phototube and $\bar{f}_i$ is the reading after correction. Depending on the energy in each cell, this correction factor generates different weighting factors. The constant A was introduced as an energy normalization parameter.

Figure 3.9 (b) shows a histogram after applying this correction, which brings the resolution to $0.5/\sqrt{E}$, which is still larger than the resolution obtained before the calorimeters were modified. The modifications to the original design which were described previously, could be a major source for this degradation of the resolution.

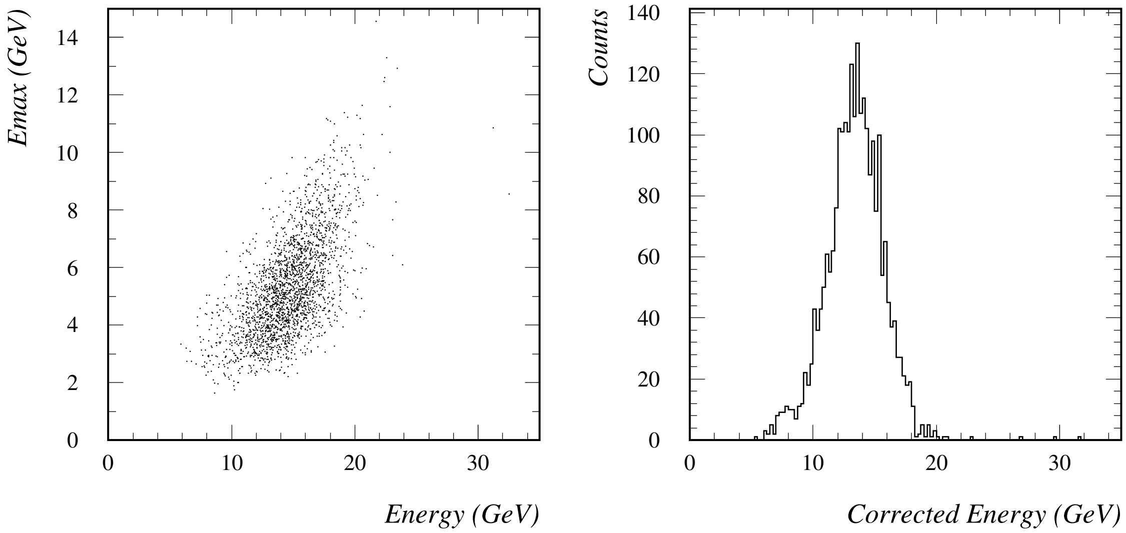

Figure 3.9: Shower fluctuations. (a) Maximum cell energy vs. the total energy. (b) Energy after correcting for the fluctuations.

C Tracking Chambers

The information from tracking chambers was processed in two steps. The first step, which is described here, deals with the preliminary pattern recognition and noise elimination, and the second step, which is described in chapter 5, deals with more rigorous analysis that pushes the chambers to their limits.

1 Pad Section

1.1 Noise corrections

In general, the noise in the pad sections of the tracking chambers does not require tedious corrections since the noise rms is only about 10-20 ADC counts in a scale where minimum ionizing particles produce a charge corresponding to about 200 ADC counts. Although there are serious noise problems in DC2 and DC3, especially in the regions where large pads are located, no attempt was made to correct these problems since they did not interfere with the regions with which this analysis is concerned. A full description of most of the noise problems in DC1 are well described in reference [55], and only the relevant problems are discussed here.

Occasionally, pads along some anode wires in DC1 reported negative signals which were large enough to wipe out the minimum ionizing signals. Figure 3.10 (a) shows an event of this type. Here, the squares represent positive signals and the circles represent negative signals. The area represents the amount of charge in each readout node. A reason for this offset could be a poor connection between the anode wire and the isolating capacitor which provides an AC ground.

This problem was corrected by taking the average of the negative signals along the

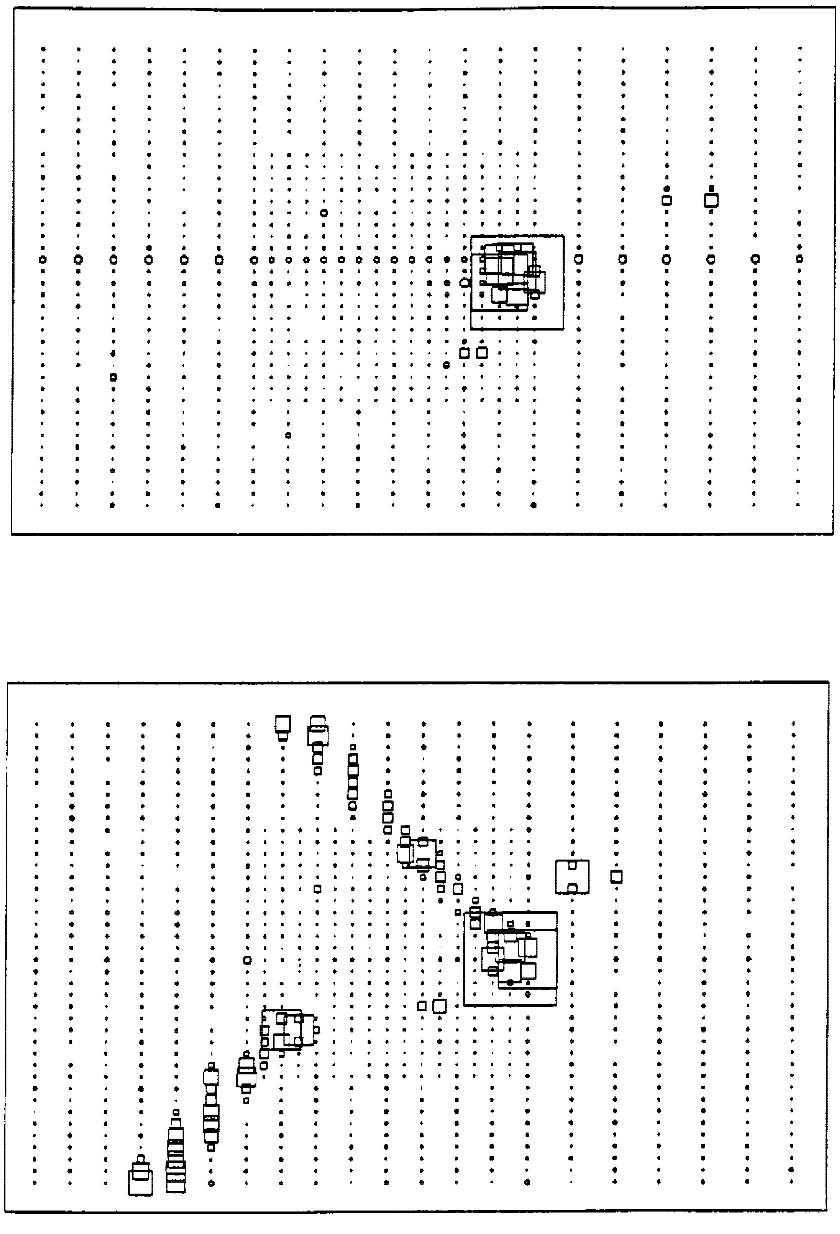

Figure 3.10: DC1 event display showing two common problems induced by the heavy ions passing through the chamber. (a) Negative signal shift along anode wire. (b) Two δ rays emerging from a heavy ion cluster. Ref [55]

anode wires in the region of the chamber where no peripheral protons were seen. For the correction, size differences in the readout nodes in different regions were taken into account. Since this problem was not observed in DC2 and DC3, no special corrections were applied to the pad sections in these chambers.

1.2 Cluster finding

The cluster finding in the pad sections were initiated by searching for single hits which deposited above 100 ADC counts. A cluster was defined as the selected hit and its two closest neighbors along the anode wire, beneath the hit pad. These two neighbors were not counted as a new cluster. A heavy ion hit produces a large amount of charge in the pad sections around the hit location. For this reason, hits inside a given window around the maximum hit for any single event, were not taken as new hits. Different size windows were used in the three chambers for this purpose. After extracting all the clusters, the total cluster charge was computed by taking the sum of the three signals. The cluster with the maximum charge was defined as the heavy ion hit.

The δ rays originating from the heavy ions make cluster finding very difficult. Figure 3.10 (b) shows an event with two δ rays originating from the heavy ion location. The amount of charge deposited by these δ rays can easily confuse the minimum ionizing signal. In addition, it can degrade the position resolution in these chambers. No corrections were applied in this analysis to correct for the effects arising from δ rays due to the poor understanding of their effect on the pad sections.

1.3 Position using the data from the Pads

An excellent description of the position estimation in pad chambers is given in reference [55]. The suggested method uses the property of charge sharing between pads which is a characteristic of this type of chamber. Figures 3.11 (a) and (b) show the charge ratio plots for heavy ions and protons passing through the chamber DC1. Here, Q_l, Q_m and Q_r define the three signals belonging to a cluster. Of these three signals the middle signal Q_m has the maximum charge. The width of the band represents the position resolution in the chamber. Any effect due to δ rays will cause the ratio to fall outside this band.

The suggested centroid finding formula for these chambers is,

$$POS = \frac{Q_{i-1}X_{i-1} + Q_iX_i + Q_{i+1}X_{i+1}}{Q_{i-1} + Q_i + Q_{i+1}}$$

assuming the charge distribution is spread over 3 readout nodes. Here, X_i and Q_i represent the position and the measured charge at readout node i.

Figure 3.12 (a) shows the position measured by the vertex detector extrapolated to the DC1 plane, against the position measured by DC1 for beam tracks taken with no target in the target holder (empty target). Figure 3.12 (b) shows the difference

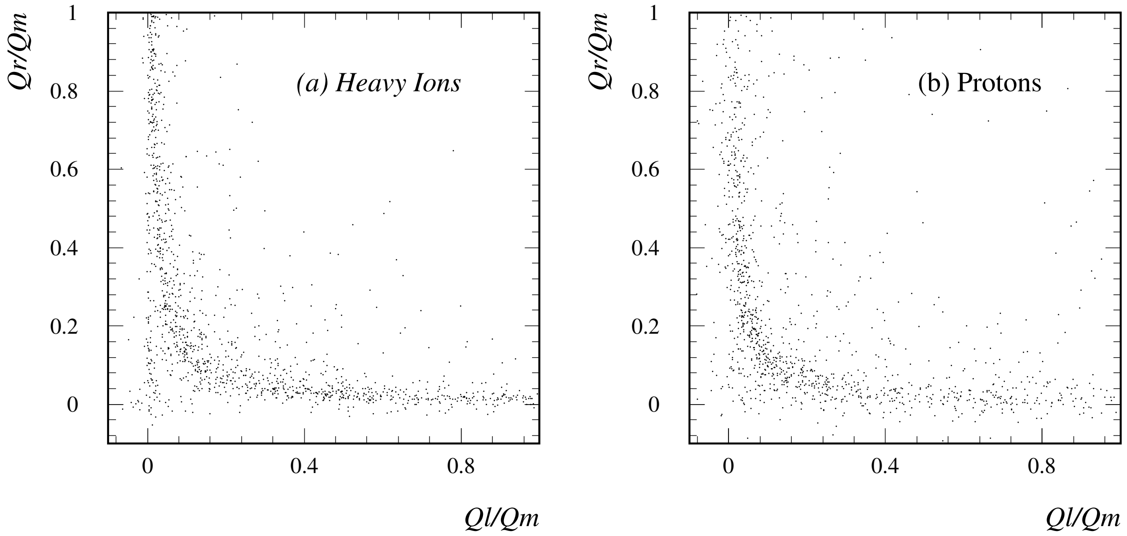

Figure 3.11: Charge ratio plot. (a) Heavy ions. (b) Protons.

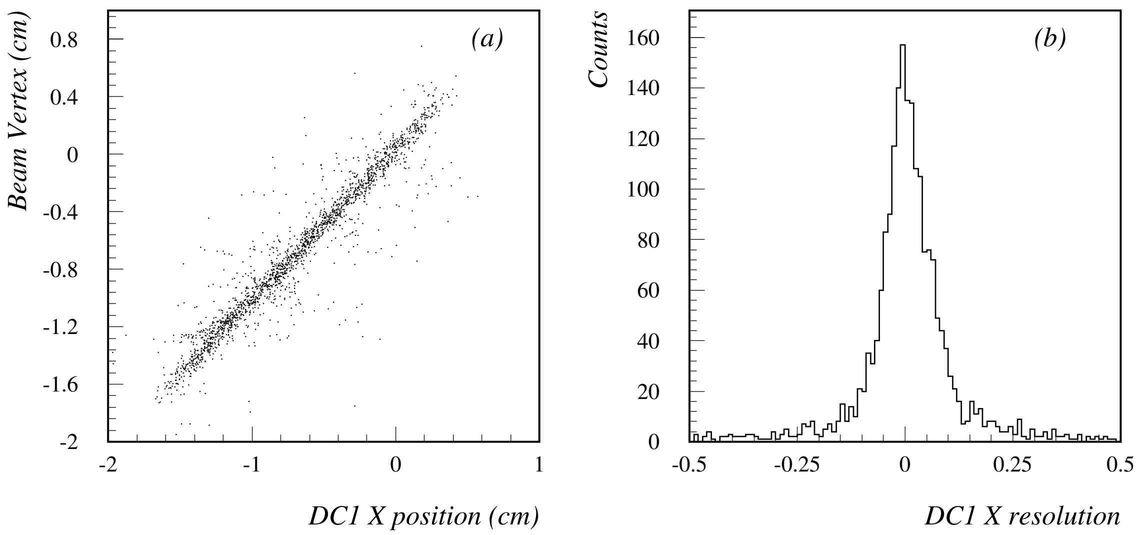

Figure 3.12: DC1 resolution in the x position measurement. (a) Beam vertex measurement extrapolated to the DC1 plane vs. the DC1 x measurement. (b) The difference between the two measurements.

between the two measurements. The width of this distribution is about 500 μm. Accounting for the contributions from multiple scattering and the vertex detector resolutions, we estimate the DC1 resolution to be about 200 μm. This value is twice the value of the expected resolution with x-ray measurements. But x-ray measurement studies show that, at higher charge levels, the position resolution is degraded due to the spreading of the avalanche along the anode wire. In addition, the δ rays adversely affect the position resolution in these chambers.

This formula is modified slightly when it is used with the chevron shaped pads in DC2 and DC3. Charge sharing between chevrons occurs mostly between two pads, and therefore only two terms were used for the position estimate. Out of the two possible pad neighbors, the pad with the higher charge was selected. Preliminary results showed that the algorithm tends to pull the position distributions towards the edge of the hit pad. In order to correct for this effect, a constant was introduced to shift the centroids and the modified formula reads,

$$POS = \frac{Q_m(X_m \pm A) + Q_s(X_s \mp A)}{Q_m + Q_s}$$

where Q_m and X_m refer to the hit pad charge and the position respectively and Q_s and X_s refer to the same quantities for its selected neighbor. The sign of the constant A was selected to pull the distributions towards the center of the hit pad and it depends on the location of the neighbor in the physical chamber with respect to the hit pad. The optimum value of A was $\sim$10% of the length of the hit pad.

Figures 3.13 (a) and (b) show the measured Y position distributions for beam tracks in DC2 and DC3 plotted against the reconstructed position distributions extrapolated to the planes of each chamber assuming the tracks pass at target Y=0. When calculating the reconstructed position, the chamber to be tested was taken out of the fit. These distributions yield us a position resolution of 2.5 mm for DC2 and 5.0 mm for DC3. These results indicate that chevrons produce a resolution which is approximately 10% of the size of the chevron.

2 Drift Section

2.1 Noise Elimination

Due to the presence of δ rays created by the heavy ion tracks, a typical peripheral event produces a large number of TDC hits in drift wires. Compared to central events, track reconstruction of peripheral events becomes rather difficult due to this reason, and this forces the offline analysis to develop fast pattern selection algorithms. These chambers were developed and constructed especially to deal with heavy ions and therefore peripheral events, with a high Z particle in the final state, can demonstrate that the chambers perform up to the expected standard.

Figure 3.14 (a) shows a histogram of observed TDC counts for wires in a single plane of DC2 for a collection of tracks produced by the presence of a single proton

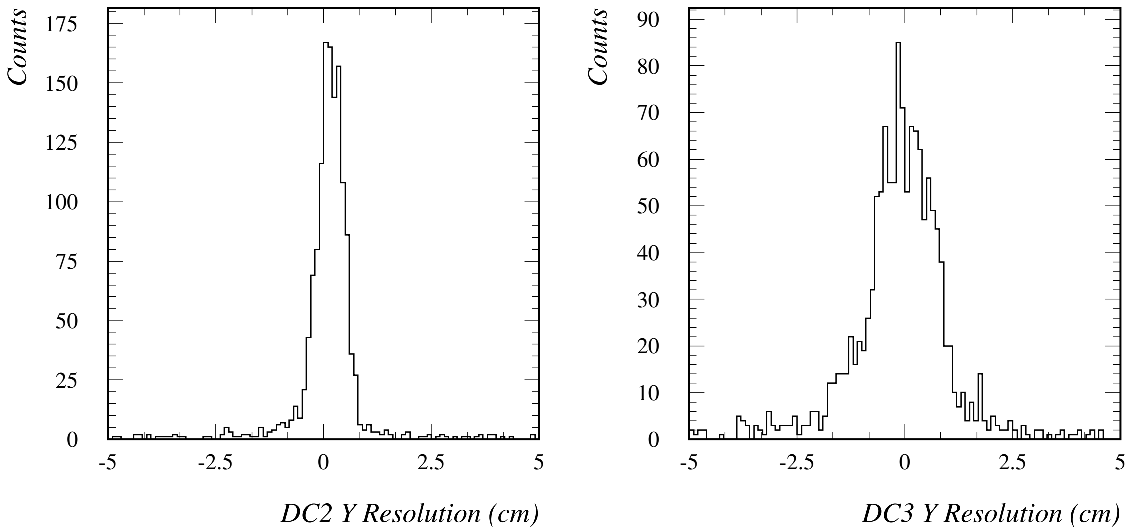

Figure 3.13: Measured y position resolution by chevron pads (a) Difference between the DC1 measurement extrapolated to the DC2 plane, and the DC2 position measurement. (b) Same for DC3.

and a heavy ion. Every wire with a "hit" makes one entry for each event. Although we can recognize the heavy ion and the proton as two distinct peaks, the background noise in the chamber makes it cumbersome to do any reliable pattern recognition without selecting genuine TDC hits that belong to the two tracks. This is specially applicable to heavy ion tracks since most of the hits that originate from δ rays appear as genuine TDC hits at first glance.

The pad plane in each drift chamber can pin-point the pad wire at which the heavy ion track traverses since it carries the information about the charge. This is a useful way to remove the uncorrelated TDC hits in the drift sections. For the heavy ion track, due to its tight rigidity, the bending angle remains close to 60 mr. This allows us to select the true TDC hits that originate from the heavy ion track, from two wires (in each drift plane) which are closest to the pad wire at which the heavy ion was seen. For other tracks, 3-4 wires were allowed, depending on the location of the track. Figure 3.14 (b) shows the same wire plane after removing the noise. The proton and heavy ion hits are clearly visible in this plot.

2.2 T_0 Corrections

For drift chambers, T_0 defines the measured time for a track passing any given drift wire at a zero distance from the wire location. Due to the time delays in the cables and the electronic modules, T_0 differs for each wire. The online calibrations described in chapter 2, are expected to provide the initial T_0 corrections to bring the drift time in different anode wires to one common scale by taking into account the differences in cable lengths, delays in electronic paths etc.

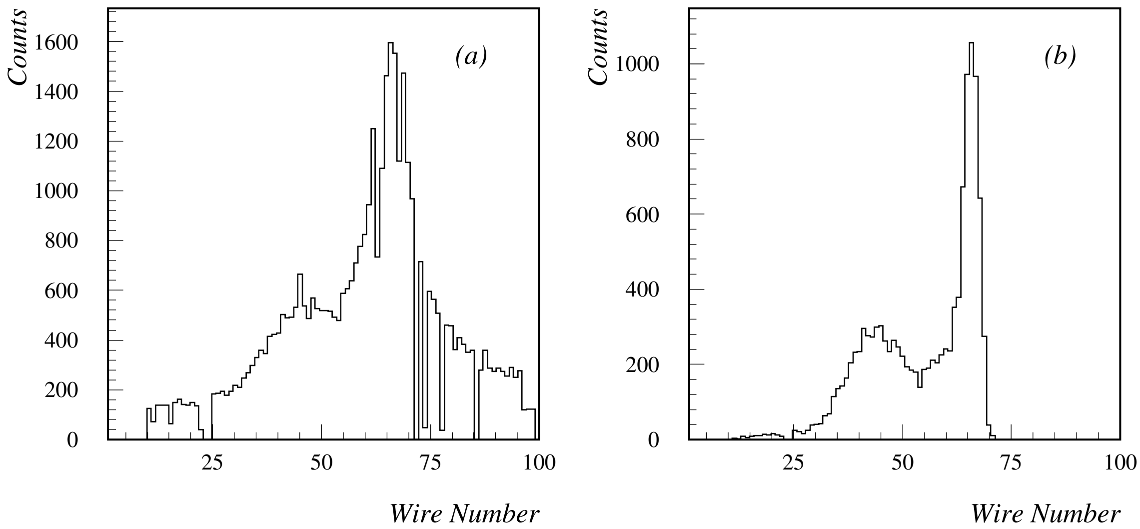

Figure 3.14: Average TDC hit distributions in drift planes in DC2. (a) Raw distribution. (b) Distribution after cleaning by a comparison with pad hits.

The T_0 constants were studied by using the peripheral protons and heavy ions. For most of the wires, the calibration constants provided very good results. For the wires for which these constants did not work, new constants were generated.

For DC2 and DC3, the T_0 values for heavy ion tracks and proton tracks differ. This could be due to the slewing effects [2] in the leading-edge discriminators since heavy ions produce much larger electron clouds than protons. To correct this effect, additional corrections of 5 nsec for DC2 and 10 nsec for DC3 were used for roughly 10 wires in each chamber where the heavy ion traversed. A variation of 3-5% was observed for T_0 constants in the two chambers.

2.3 Non-linearity in Drift Cells

To convert the timing signals to position, the following formula was used,

$$POS = V_d(T - \eta) + \Delta$$

which is a linear relation. Here, T is the measured timing, V_d is the drift velocity, and η and Δ are offset constants. Δ was introduced to correct for the shift between planes which is 0.0 for odd numbered planes in each chamber, and 0.3175 cm for DC2 and 0.6350 cm for DC3, for even numbered planes. V_d and η are 0.52 cm/nsec and 245 nsec for DC2 and 0.52 cm/nsec and 280 nsec for DC3 respectively. The observed drift times for drift cells in DC2 and DC3 were 60 nsec and 120 nsec respectively.

Although the used formula is a linear relationship between time and position, the drift time has a non-linear behavior. Figure 3.15 shows field lines and equipotential

[2] see section 4.1 in this chapter

lines for a double cell in the drift section. The tracks which pass the chamber at the boundaries take much longer to reach the anode wires. Figures 3.16 (a) and (b) demonstrate this behavior for beam tracks passing through chambers DC2 and DC3 respectively. Here, the position was estimated by assuming a uniform track density from the center of any given drift cell to its edge.

For the data analyzed here, no corrections were applied to correct for this non linearity.

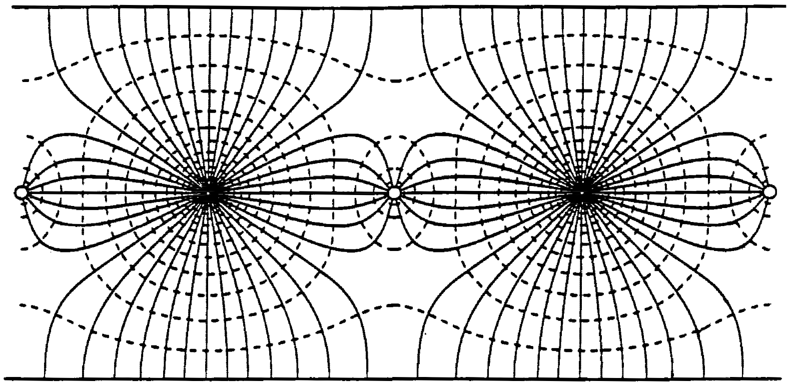

Figure 3.15: Equipotential and field lines for drift cells used in DC2 and DC3 chambers. Ref [55]

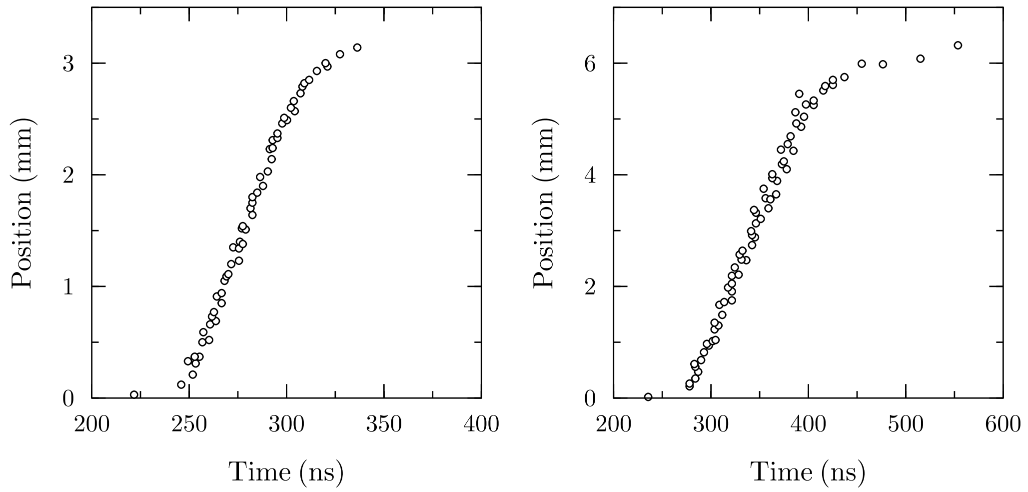

Figure 3.16: Non linearity in drift time measurement. (a) Track location vs. drift time for DC2. (b) Same for DC3.

2.4 High Level TDC information

E814 tracking chambers have a unique feature to produce two or more TDC hits from the same charge cloud. The first signal is generated by a leading-edge discriminator whereas the succeeding signals are generated by a zero-crossing discriminator. [3] The zero-crossing discriminator thresholds were set so that they do not respond to charge clouds originating from minimum ionizing tracks and hence true heavy ion hits can be selected by omitting the noise signals from δ rays.

In preliminary pattern recognition, second hits or so called high level TDC information was not used. A discussion on how these could be used to help pattern recognition is given later.

[3] see chapter 2, section 3.3

CHAPTER 4

Selection of Electromagnetic Interactions

In this chapter, a full description of the peripheral trigger setup, the data reduction methods and the cross section estimations for simple decay channels produced by electromagnetic interactions is given. This analysis was later combined with a more rigorous analysis developed to study complex decay channels.

A Online Selection

As described in chapter 2, the main purpose of the trigger is to make fast, reliable decisions about given events, whether they should be accepted or not, by studying the limited number of signals obtained from various detector systems. An efficient trigger allows the data acquisition system to store only the interesting events and it does not waste time over uninteresting events.

1 Peripheral Trigger

The selection criteria for the peripheral trigger is based on the selection of events which produce low activity in the target region detectors. In addition, to reduce the background and to enhance each event type, the trigger was set up to select events with a substantial charge in the heavy ion region ($Z/A \approx 1/2$) and energy in the proton and neutron region calorimeters. The selections varied depending on the type of trigger that was used.

The trigger takes about 20 μsec of processing time to analyze a peripheral event. Due to the beam rates used in our experiment ($\sim 10^5$ particles/sec) the beam particles are spaced by only a few μsec. Thus, it is not possible for the trigger to analyze and make decisions about every beam particle fully. Due to this reason, the trigger was implemented in several parallel processing stages [37] with different processing times that depend on the number of elements used in the trigger decision. As a result, no time was wasted over events which were identified as uninteresting events, and only the events which were good candidates for a given physical process were analyzed fully before the final decision was made. A description of each type of trigger is given below.

- *Beam triggers* – Beam triggers are the most unbiased triggers in the experiment and are very useful for measuring efficiencies of more complex triggers. They are defined by the signals extracted from the 4 beam scintillators S1-S4. Good ^{28}Si beams are identified by the pulse height corresponding to Z=14 in S2 and S4 with no hits recorded by S1 and S3.

- *Pre-triggers* – The pre-trigger is the first signal which indicates that a possible interaction has occurred. This is formed by the coincidence of the beam trigger and the energy sum in the proton or the neutron region calorimeters. The pre-trigger initiates the process of digitizing information from all detectors, including the FERA ADC's which are used in the second level trigger. The pre-trigger can be taken as a "minimum bias" trigger for most of our applications. These events are also useful in studying efficiencies, as they are richer in interesting events compared to the beam triggers.

- *First Level trigger* – The purpose of the first level trigger is to look for beam particles which are closer than 1μsec from the previous beam particle. If the pre-trigger is generated by such a particle, it will send CLEAR signals to all the detectors in the experiment to abort the digitization and to be ready for the next event (after protection).

- *Second Level trigger* – The second level trigger makes the final decision based on the FERA data about a given event. In the case of peripheral triggers, the information from the target region veto detectors (multiplicity detector, downstream veto wall, participant calorimeter, target calorimeter, and magnet scintillators) and the downstream detectors (downstream silicon detector, downstream forward scintillators, and the energy sum in calorimeter modules) was used. The triggers generated with the aid of all the detectors listed above were marked as triggers with online vetos and the triggers generated without the target region detectors but using the downstream calorimeters and forward scintillators were marked as triggers without online vetos.

- *Parallel Triggers* – The E814 data acquisition can accept only up to 30 events per spill. If individual triggers have rates higher than this, the events which are more abundant would be collected more frequently. To prevent this, the trigger system was designed to allow data taking with parallel triggers, with the ability to accept only a fraction of the triggers in any given channel (we call this process "downscaling"). In this manner we are able to enhance rare event types.

In addition to the second level trigger, several other triggers were activated to study gain variations and other systematic effects. They are the beam triggers, the pre-triggers and the MT triggers (random triggers with no beam particle present, generated through a random pulser). The frequency of these triggers were adjusted